

# Simulation of solid deformation during solidification: Shearing and compression of polycrystalline structures

M. Yamaguchi, C. Beckermann\*

*Department of Mechanical and Industrial Engineering, The University of Iowa, Iowa City, IA 52242, USA*

Received 24 October 2012; received in revised form 27 December 2012; accepted 31 December 2012

Available online 4 February 2013

## Abstract

Deformation of the semi-solid mush during solidification is a common phenomenon in metal casting. At relatively high fractions of solid, grain boundaries play a key role in determining the mechanical behavior of solidifying structures, but little is known about the interplay between solidification and deformation. In the present study, a polycrystalline phase-field model is combined with a material point method stress analysis to numerically simulate the coupled solidification and elasto-viscoplastic deformation behavior of a pure substance in two dimensions. It is shown that shearing of a semi-solid structure occurs primarily in relatively narrow bands near or inside the grain boundaries or in the thin junctions between different dendrite arms. The deformations can cause the formation of low-angle tilt grain boundaries inside individual dendrite arms. In addition, grain boundaries form when different arms of a deformed single dendrite impinge. During compression of a high-solid fraction dendritic structure, the deformations are limited to a relatively thin layer along the compressing boundary. The compression causes consolidation of this layer into a fully solid structure that consists of numerous sub-grains. It is recommended that an improved model be developed for the variation of the mechanical properties inside grain boundaries. © 2013 Acta Materialia Inc. Published by Elsevier Ltd. All rights reserved.

*Keywords:* Polycrystalline solidification; Viscoplastic deformation; Phase-field method; Material point method; Grain boundaries

## 1. Introduction

Deformation of the semi-solid mush is a common phenomenon in solidifying metal castings. It can lead to defects, such as hot tears, macrosegregation and porosity [1]. Therefore, understanding the mechanical behavior of the mush during solidification of metal alloys is of great importance in casting simulations incorporating a stress analysis [2]. In the first part of the present study [3], a model was developed to simulate the coupled solidification and deformation of a single dendrite of a pure substance in two dimensions. The phase-field method [4,5] was used to model dendritic solidification, while the material point method [6] was used to compute the stresses and elasto-viscoplastic deformation of the solid. The flow of the liquid was not simulated and the solid–liquid interface was

assumed to be stress free. In the material point method, Lagrangian point masses are moved through a fixed Eulerian background mesh. Hence, the material point method is well suited for simulating large deformations and also for coupling with the Eulerian phase-field method. However, the issue of contact and bridging between different portions of a deformed dendrite was not addressed in Ref. [3]. Such impingement can lead to the formation of grain boundaries, even for a single crystal. The formation of grain boundaries between two or more crystals having different crystallographic orientations was not treated.

In the present paper, the model of Ref. [3] is extended to consider polycrystalline structures. Grain boundaries play an important role in the deformation of a mush, especially at high volume fractions of solid. For example, they can delay the formation of solid bridges between dendrites. Not surprisingly, hot tears due to tensile strains in a mushy zone usually form at grain boundaries [7,8]. The inelastic deformation of multi-grain and dendritic microstructures

\* Corresponding author. Tel.: +1 319 335 5681; fax: +1 319 335 5669.  
E-mail address: [becker@engineering.uiowa.edu](mailto:becker@engineering.uiowa.edu) (C. Beckermann).

has been simulated in a few recent studies [9,10], but those studies did not consider solidification and the dynamics of grain boundaries. Sistaninia et al. [11] developed a three-dimensional (3-D) granular model to study the mechanical behavior of a semi-solid mush at high fractions of solid. Although solidification of the initial grain structure was simulated in Ref. [11], the subsequent stress analysis was uncoupled. Clearly, the microstructure of the solid plays a key role in the mechanical behavior of a mush. But solid deformations can also affect the evolution of the solid morphology by solidification and grain boundary dynamics. For example, a new grain boundary can form when a severely deformed dendrite arm grows into an undeformed portion of the same dendrite. Furthermore, new tilt grain boundaries can form when a dendrite arm is bent.

The grain boundaries are simulated in the present study using the polycrystalline phase-field model of Warren et al. [12]. As in all phase-field models, the phase-field parameter  $\phi$  is used to indicate the local crystalline order, with  $\phi = \pm 1$  inside the bulk solid and liquid phases, respectively. The solid–liquid interface is treated as a diffuse layer of small but finite thickness over which the phase field varies smoothly between  $\phi = \pm 1$ . The grain boundary between two solid grains is also treated as a diffuse interface. Since the crystalline order inside a grain boundary is reduced, the phase field assumes values below unity (solid) within the grain boundary. An additional order parameter, the crystal orientation angle field  $\alpha$ , is introduced to measure the local crystallographic orientation of the solid with respect to a fixed coordinate system. If two neighboring grains are mis-oriented, the orientation angle varies smoothly across the diffuse grain boundary from the value in one grain to the value in the other grain. The misorientation,  $\Delta\alpha$ , is given by the integral of the orientation angle gradient,  $\nabla\alpha$ , across the grain boundary. The phase field and the orientation angle are closely coupled inside a grain boundary. The larger the angle gradient (or misorientation), the lower the minimum value of the phase field. At some critical misorientation, the minimum value of the phase field reaches  $\phi = -1$  and the grain boundary is fully wet. The model of Warren et al. [12] also considers the anisotropy in the interfacial energy, which is essential for modeling dendritic solidification. They demonstrated that the model correctly predicts phenomena such as triple junction behavior, the wetting condition for a grain boundary, curvature-driven grain boundary motion and grain rotation.

In the present paper, the polycrystalline phase-field model of Warren et al. [12] is modified to account for deformation of the solid. Several numerical examples are presented to show that the model is correctly implemented. The reader is referred to the companion paper [3] for a description and detailed validation tests of the material point method for the stress and deformation calculations. A highly simplified description is used for the mechanical behavior of a grain boundary. A solid bridge between two adjoining crystals is assumed to be formed when  $\phi > 0$  inside a grain boundary. Conversely, for values of  $\phi$

$< 0$ , the grain boundary is assumed to contain sufficient liquid-like material that it can be considered wet and no stresses are transmitted between the two crystals. The ability of the present model to simulate deformation of polycrystalline semi-solid structures is demonstrated in several numerical examples.

## 2. Polycrystalline phase-field method for dendritic solidification with solid deformation

The polycrystalline phase-field model for solidification of Warren et al. [12] is extended here to include a deformation velocity field,  $\mathbf{v}$ . It is also modified to reduce exactly to the quantitative phase-field model of Karma and Rappel [13] for a single dendrite, since that version was used in the first part of the present study [3].

Let  $\phi$  denote the phase field, where  $\phi = \pm 1$  refers to the bulk solid and liquid phases, respectively. The anisotropic form of the two-dimensional (2-D) polycrystalline phase-field evolution equation is given by [12]

$$\begin{aligned} \tau_\phi(\psi - \alpha) \left( \frac{\partial \phi}{\partial t} + \mathbf{v} \cdot \nabla \phi \right) = & \nabla \cdot [W^2(\psi - \alpha) \nabla \phi] - \frac{\partial f(\phi, \lambda \theta)}{\partial \phi} \\ & + \frac{\partial}{\partial x} \left[ |\nabla \phi|^2 W(\psi - \alpha) \frac{\partial W(\psi - \alpha)}{\partial \phi_x} \right] \\ & + \frac{\partial}{\partial y} \left[ |\nabla \phi|^2 W(\psi - \alpha) \frac{\partial W(\psi - \alpha)}{\partial \phi_y} \right] \\ & - \frac{\partial g(\phi)}{\partial \phi} s |\nabla \alpha| - \frac{\partial h(\phi)}{\partial \phi} \frac{e^2}{2} |\nabla \alpha|^2 \end{aligned} \quad (1)$$

The above equation is similar to the phase-field equation used in the companion paper [3] for a single dendrite, except for the addition of the last two terms on the right-hand side. These terms account for the effect of crystal orientation angle gradients,  $|\nabla \alpha|$ , on the phase field. In the presence of solid deformation, such gradients exist not only inside grain boundaries but also inside grains. Inside the last two terms in Eq. (1),  $g(\phi) = h(\phi) = [(1 + \phi)/2]^2$  are monotonically increasing functions and  $s$  and  $e$  are angle gradient coefficients that can be related to grain boundary properties (see below) [12]. The above phase-field equation also includes anisotropy in the surface energy of a crystal. Following the methodology of Warren et al. [12], the anisotropic phase-field relaxation time and diffuse interface thickness parameter are given by  $\tau_\phi(\psi - \alpha) = \tau_0 \xi^2(\psi - \alpha)$  and  $W(\psi - \alpha) = W_0 \xi(\psi - \alpha)$ , respectively, where the four-fold anisotropy function is given by  $\xi(\psi - \alpha) = 1 + \varepsilon \cos[4(\psi - \alpha)]$  and  $\varepsilon$  is the anisotropy strength. The “inclination” [10] angle of the interface with respect to the  $x$ -axis is given by  $\psi = \tan^{-1}(\phi_y/\phi_x)$ . The above procedure ensures that the anisotropy is computed in the crystal-line frame. To be consistent with the phase-field model of Karma and Rappel [13] and Ref. [3], the phenomenological bulk free energy function is taken to be  $f(\phi, \lambda \theta) = q(\phi) + \lambda \theta p(\phi)$ , in which  $q(\phi) = -\phi^2/2 + \phi^4/4$  is a double-well function and  $p(\phi) = \phi - 2\phi^3/3 + \phi^5/5$  is

an odd function. The dimensionless temperature is given by  $\theta = (T - T_m)/(L/c_p)$ , in which  $T$ ,  $T_m$ ,  $L$  and  $c_p$  are the temperature, melting point, latent heat and specific heat, respectively.

The evolution equation for the angle field,  $\alpha$ , is given by [12]

$$P(e|\nabla\alpha|)\tau_\alpha\left(\frac{\phi+1}{2}\right)^2\left(\frac{\partial\alpha}{\partial t}+\mathbf{v}\cdot\nabla\alpha-\nabla\times\mathbf{v}\right) = \nabla\cdot\left[\left(\frac{g(\phi)s}{|\nabla\alpha|}+h(\phi)e^2\right)\nabla\alpha\right] \quad (2)$$

where  $\tau_\alpha$  is a kinetic scaling factor for the angle field and  $P(e|\nabla\alpha|)$  is an inverse mobility function. The latter is given by  $P(w) = 1 - (1 + \mu/e) \exp(-\beta w)$ , where  $\mu$  and  $\beta$  are coefficients that independently control the angle relaxation time in the bulk grain and grain boundary regions (see below) [12]. Setting the right-hand side of Eq. (2) equal to zero results in the same angle evolution equation as used in the first part of the present study [3]; that equation accounts for advection and rotation of the angle field by the deformation velocity,  $\mathbf{v}$ . The right-hand side of Eq. (2) is a diffusion term that governs both the variation of the angle inside a static grain boundary and the evolution of the angle field in the presence of grain boundary motion. Due to the presence of the  $1/|\nabla\alpha|$  term, the diffusivity in Eq. (2) can be singular; this problem is resolved using the same cut-off function approach as in Appendix B.2 of Ref. [12]. The  $2\pi$  periodicity in the angle field is accounted for using the same method as in Appendix B.3 of Ref. [12]. Warren et al. [12] note in Appendix B.4 of their paper that although the crystalline orientation angle variable  $\alpha$  has no meaning in the liquid phase, a value still needs to be assigned since Eq. (2) is solved over the entire domain. In the present study, as already described in the first part of the present study [3], the orientation angle is numerically extended into the liquid using the PDE-based zero-gradient extension scheme of Gibou et al. [14]. While there is no physical meaning associated with this procedure, it results in the liquid having an orientation angle equal to the one of the closest solid.

Finally, the temperature field is obtained from the following heat equation:

$$\frac{\partial\theta}{\partial t}+\mathbf{v}\cdot\nabla\theta=D\nabla^2\theta+\frac{1}{2}\left(\frac{\partial\phi}{\partial t}+\mathbf{v}\cdot\nabla\phi\right)+c(\theta_0-\theta) \quad (3)$$

where  $D$  is the thermal diffusivity. The last term in Eq. (3) is a volumetric heat sink that is included in some simulations to allow for complete solidification of a domain with adiabatic boundaries [12]. The coefficients  $c$  and  $\theta_0$  are used to control the rate and magnitude of the heat sink.

The above equations are non-dimensionalized using  $W_0$  and  $\tau_0$  as the length and time scales, respectively. The coupling constant,  $\lambda$ , in Eq. (1) is chosen in accordance with the thin-interface analysis of Karma and Rappel [13] in order to model kinetics-free solidification. In this method, the coupling constant is given by  $\lambda = a_1 W_0/d_0$ , where  $d_0$  is the solid–liquid capillary length and  $a_1 = 0.8839$  for the functional forms of  $q(\phi)$  and  $p(\phi)$  given above. The kinetic

effect vanishes when  $\tau_0 = a_1 a_2 (W_0)^3/(d_0 D)$ , where  $a_2 = 0.6267$ . Only  $W_0$  is a free parameter that has to be reduced until a converged solution that is independent of the diffuse interface thickness is obtained. Reducing  $W_0$  also necessitates the use of a finer numerical grid in order to resolve the steep variation of the phase field inside the diffuse interface; here, the grid spacing is kept at  $\Delta x/W_0 = 0.4$ . A dimensionless thermal diffusivity of  $D\tau_0/W_0^2 = 3$  and a dimensionless capillary length of  $d_0/W_0 = 0.185$  are used throughout this study [3]. The polycrystalline phase-field model of Warren et al. [12] introduces a number of additional parameters that control the statics and dynamics of grain boundaries:  $\tau_\alpha$ ,  $\mu$ ,  $\beta$ ,  $e$ , and  $s$ . The present choices for these parameters are guided by the considerations and asymptotic results of Warren et al. [12]; they do not correspond to a specific material. The kinetic scaling factor for the angle is chosen as  $\tau_\alpha = 0.1\tau_0$ . The coefficients in the inverse mobility function are taken as  $\mu = 10^3 W_0$  and  $\beta = 10^5$ . Warren et al. [12] show in a one-dimensional analysis of a static ( $e = 0$ ) grain boundary at the melting point that the first angle gradient coefficient  $s$  controls the critical misorientation  $\Delta\alpha_c$  between two crystals through a relation of the form  $\Delta\alpha_c = W_0/s$ . For misorientations larger (smaller) than this critical value, the grain boundary between the two crystals is wet (dry). In the present study we choose  $s = W_0/1.06$ , giving a critical misorientation for a static grain boundary of  $\Delta\alpha_c = 1.06 = 67.5^\circ$ . The second angle gradient coefficient  $e$  controls grain boundary motion and is set to  $e = W_0/1.875$  [12]. Again, the above choices for the parameters in the polycrystalline phase-field model are essentially adopted from Warren et al. [12], and the reader is referred to that study for an examination of the effect of variations in the model parameters on the results.

The deformation velocity of the solid,  $\mathbf{v}$ , is obtained from the material point method stress model [6]. The main feature of this method is that it uses a Lagrangian description for the motion of material points and a fixed Eulerian background mesh for solving the equation of motion. The use of Lagrangian material points makes the material point method well suited for large material deformations, where traditional finite element methods would suffer from mesh collapse or entanglement problems. The fixed Eulerian background mesh is the same as the one used in the solution of the phase-field model equations. The reader is referred to the companion paper [3] for a more detailed description of this method and its application to the deformation of a single dendrite. The material point method implemented in the present study is intended for elasto-viscoplastic materials, but all computations in this paper are limited, for simplicity, to an elasto-perfectly plastic material. The mechanical properties used are given by a Young's modulus of  $E = 50$  GPa, a Poisson ratio of  $\nu = 0.33$ , and a yield stress of  $\sigma_Y = 5$  MPa. These values are not intended to represent a particular material, but are reasonably close to those of metals near the melting point [2].

As described in the companion paper [3], the stress model is only solved in that region of the computational domain that is solid. The zero contour of the phase field is taken as the solid–liquid interface and, hence, defines the boundary of the solid at any point in time. The solid–liquid interface is treated as stress free. In other words, stresses from the liquid are neglected. In fact, the flow of the liquid is not at all modeled in the present study. However, since Eqs. (1)–(3) are solved over the entire computational domain, a velocity field is needed everywhere. As in Ref. [3], the velocities in the liquid are calculated by a zero-gradient extension of the solid velocity in the direction normal to the solid–liquid interface, i.e., the liquid at any point in space and time has the same velocity as the closest solid. Again, the PDE based scheme of Gibou et al. [14] is used to perform the velocity extension.

Special consideration must be given to the mechanical behavior of a grain boundary. It is known that the strength of low-angle grain boundaries ( $\Delta\alpha$  less than  $\sim 0.2 \approx 11^\circ$ ) decreases with increasing misorientation between the grains. For high-angle grain boundaries ( $\Delta\alpha$  greater than  $\sim 0.2 \approx 11^\circ$ ), the bonds between the grains are weakened further, but the properties are normally unrelated to the misorientation. In both cases, the reductions in the strength can be attributed to the reduced crystalline order inside a grain boundary. Above the critical misorientation,  $\Delta\alpha_c$ , the grain boundary is wet and has no strength. Crystals separated by a wet grain boundary would be able to slide against each other and could be pulled apart easily. Based on these considerations, the local mechanical properties inside a grain boundary may be related directly to the value of the phase field,  $\phi$ , since it is a measure of the local crystalline order. Recall that inside a grain boundary the phase field assumes values below unity. However, quantitative relations between mechanical properties, such as the elastic modulus or the yield strength, and the value of the phase field inside a grain boundary, are currently not available. Therefore, a highly simplified procedure is adopted in the present study to model these effects. When the value of the phase field is greater than zero ( $\phi > 0$ ), the material inside a grain boundary is assumed to behave mechanically like a solid and material points are assigned to that computational cell in the material point method stress analysis. Hence, a grain boundary becomes mechanically bridged (by solid) as soon as the minimum value of the phase field inside the grain boundary exceeds zero. Conversely, for  $\phi < 0$  the material is treated in the stress analysis as a liquid. In other words, a grain boundary is assumed to behave mechanically like a liquid when the minimum value of the phase field inside the grain boundary is below zero, even though it is not fully wetted until the minimum value reaches  $\phi = -1$ . In the presence of liquid-like material ( $-1 < \phi < 0$ ) inside a grain boundary, no stresses are transmitted between the two crystals, because the stress model is only solved in cells that are solid and the stresses in the liquid are not calculated (i.e., they are zero). Clearly, a more sophisticated model should be developed that solves

for the stresses not only in the solid but also in the liquid. Such a model could incorporate phase-field-dependent mechanical properties reflecting the weakening of the solid due to reduced crystalline order inside a grain boundary. The above procedure for modeling the mechanical behavior of a grain boundary is consistent with the method used in the present study to treat the solid–liquid interface in the stress analysis. As mentioned above, the switch from solid to liquid is also made at the zero phase-field contour.

### 3. Numerical procedures and tests

The model described in the previous section is solved using the same numerical methods as described in the companion paper [3]. The only new terms are the two orientation angle gradient-dependent terms in Eq. (1) and the diffusion term on the right-hand side of Eq. (2). These terms are discretized using the implicit method described in Appendix B of Warren et al. [12]. The advection and diffusion terms are solved sequentially, using different time steps, by employing the fractional step or operator splitting approach [15]. The third-order accurate CIP method [16] is used for discretizing the advection terms (i.e., those involving  $\mathbf{v} \cdot \nabla$ ).

Numerous tests of the present numerical procedures are presented in Ref. [3]. These include validations of the phase-field method for solidification of a single crystal into an undercooled melt, the phase-field advection algorithm, solidification with a prescribed deformation velocity field and the stress model for large deformations without solidification. In the following, three numerical tests are presented that focus solely on the polycrystalline aspects of the model.

#### 3.1. Liquid-grain boundary dihedral angle

In the first validation case, the wetting behavior of a grain boundary is examined in the same manner as in Section 4.2 of Warren et al. [12]. As illustrated in Fig. 1, a grain boundary forms between two adjoining grains of different crystallographic orientations immersed in melt. In two dimensions, a dihedral angle,  $\xi_{di}$ , can be defined between the solid–liquid interfaces at the junction with the grain boundary. The dihedral angle is given by Young's law according to

$$\cos\left(\frac{\xi_{di}}{2}\right) = \frac{\gamma_{bc}}{2\gamma_{ls}} \quad (4)$$

where  $\gamma_{bc}$  is the bicrystal energy of the grain boundary and  $\gamma_{ls}$  is the liquid–solid interface energy. In the phase-field model of Warren et al. [12], the bicrystal energy is potentially different from the familiar grain boundary energy due to the presence of undercooled liquid-like material inside the grain boundary. Using the expressions provided by Warren et al. [12] for the surface energies, the dihedral angle can also be expressed in terms of the misorientation,  $\Delta\alpha$ , between the two grains as

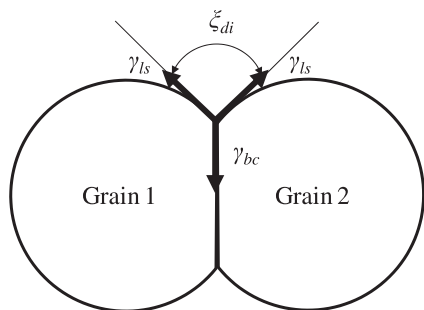


Fig. 1. Two misoriented grains forming a grain boundary inside a melt. The dihedral angle is evaluated at the triple point between the grains and the liquid, as indicated in the figure.

$$\cos\left(\frac{\zeta_{di}}{2}\right) = 1 - \left(1 - \frac{\Delta\alpha}{\Delta\alpha_c}\right)^3 \quad (5)$$

The dihedral angle is computed with the present polycrystalline phase-field model by placing two circular solid grains of different orientations ( $\alpha = \pm\Delta\alpha/2$ ) inside an adiabatic computational domain filled with melt ( $800 \times 400$  nodes). Anisotropy is not considered ( $\varepsilon = 0$ ). The grains are initially placed a small distance apart and the initial temperature is set everywhere to the melting point ( $\theta = 0$ ). The system is then allowed to evolve in time until a final steady state is achieved. If the grains have the same orientation, some phase change will take place and, after a long time, coarsening will lead to a single circular grain with the final melt undercooling determined by the curvature of the grain. For a finite misorientation, the presence of a grain boundary would prevent a single grain from forming and the solid equilibrates to a shape similar to the one shown in Fig. 1.

Fig. 2 shows the computed final phase-field contours for four different misorientations between the two grains:  $\Delta\alpha/\Delta\alpha_c = 0.19, 0.38, 0.57$  and  $1.5$ . For the smallest misorientation, the presence of a grain boundary can be discerned by

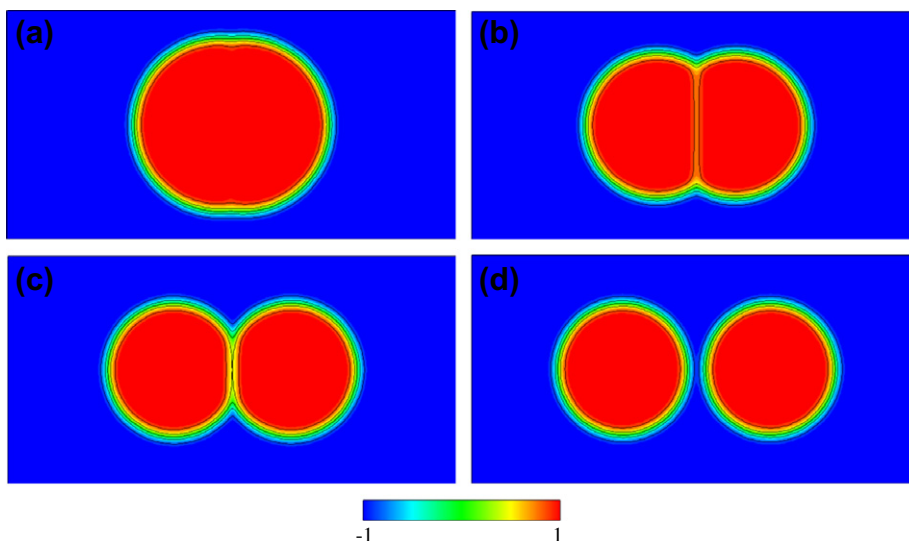


Fig. 2. Computed steady-state phase-field contours for two impinging grains in an undercooled liquid. The solid lines correspond to the  $\phi = -0.8, -0.4, 0.0, 0.4$  and  $0.8$  contours. (a)  $\Delta\alpha/\Delta\alpha_c = 0.19$ , (b)  $\Delta\alpha/\Delta\alpha_c = 0.38$ , (c)  $\Delta\alpha/\Delta\alpha_c = 0.57$ , (d)  $\Delta\alpha/\Delta\alpha_c = 1.5$ .

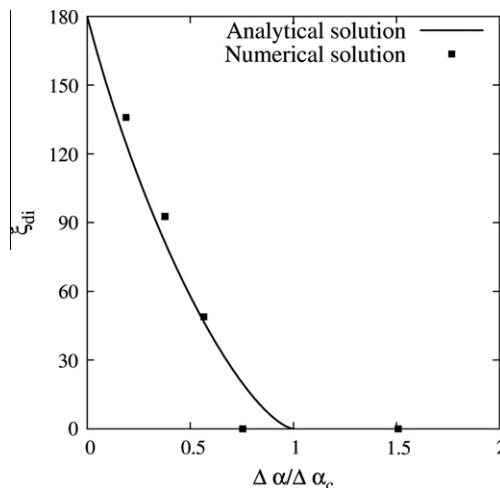


Fig. 3. Comparison of the dihedral angle measured from the phase-field simulations with the analytical prediction given by Eq. (5) as a function of the misorientation.

the neck in the otherwise circular shape of the solid. On the other hand, for the largest misorientation, the grain boundary is fully wetted and the two grains remain completely detached and circular. With increasing misorientation, the minimum value of the phase field within the grain boundary decreases as expected. The dihedral angle was measured from the phase-field results by fitting a true circle to the  $\phi = 0$  contour of the two grains in the region away from the grain boundary. The dihedral angle is then easily obtained from the position of the centers and radii of the two overlapping circles. Fig. 3 shows a comparison of the measured dihedral angles with the analytical prediction given by Eq. (5). As in Warren et al. [12], generally good agreement can be observed. The transition to full wetting, which occurs theoretically at  $\Delta\alpha/\Delta\alpha_c = 1$ , is somewhat smeared out in the phase-field computations. A fifth simulation was conducted for  $\Delta\alpha/\Delta\alpha_c = 0.75$  (not shown in

Fig. 2), and the dihedral angle was measured to be equal to zero. This discrepancy may be attributed to the difficulty of measuring the dihedral angle accurately when  $\xi_{di} \rightarrow 0$  and the possibility that the computations may not be fully converged with respect to the diffuse interface thickness.

### 3.2. Mechanical behavior of a grain boundary under tension

In the second test case, two adjoining misoriented grains are pulled apart. This test is intended to verify the present treatment of the mechanical behavior of a grain boundary. The computational domain consists of a rectangle ( $400 \times 1200$  nodes) with adiabatic boundaries. Initially, the domain contains an undercooled liquid having a dimensionless temperature of  $\theta_i = -0.55$ , except for a thin

horizontal layer of solid ( $\varepsilon = 0$ ) at the melting point evenly spread across the bottom wall. The solid layer is divided into two halves, with the left and right portions having crystallographic orientation angles equal to  $\alpha = \pm\Delta\alpha/2$ , respectively. Two simulations (a and b) are performed where the misorientation  $\Delta\alpha/\Delta\alpha_c$  is set to (a) 1.39 and (b) 0.13. Since the liquid is undercooled, the solid will grow freely upwards. The upper panels of Fig. 4 show the computed phase-field contours after the solid has grown upward by  $\sim 150$  node points (the upper half of the domain is truncated in this figure). As expected, a grain boundary forms between the two grains along the vertical centerline of the domain. Some of the undulations on the solid–liquid interface can be attributed to the grain boundary. For the higher misorientation ( $\Delta\alpha/\Delta\alpha_c = 1.39$ ), the grain boundary

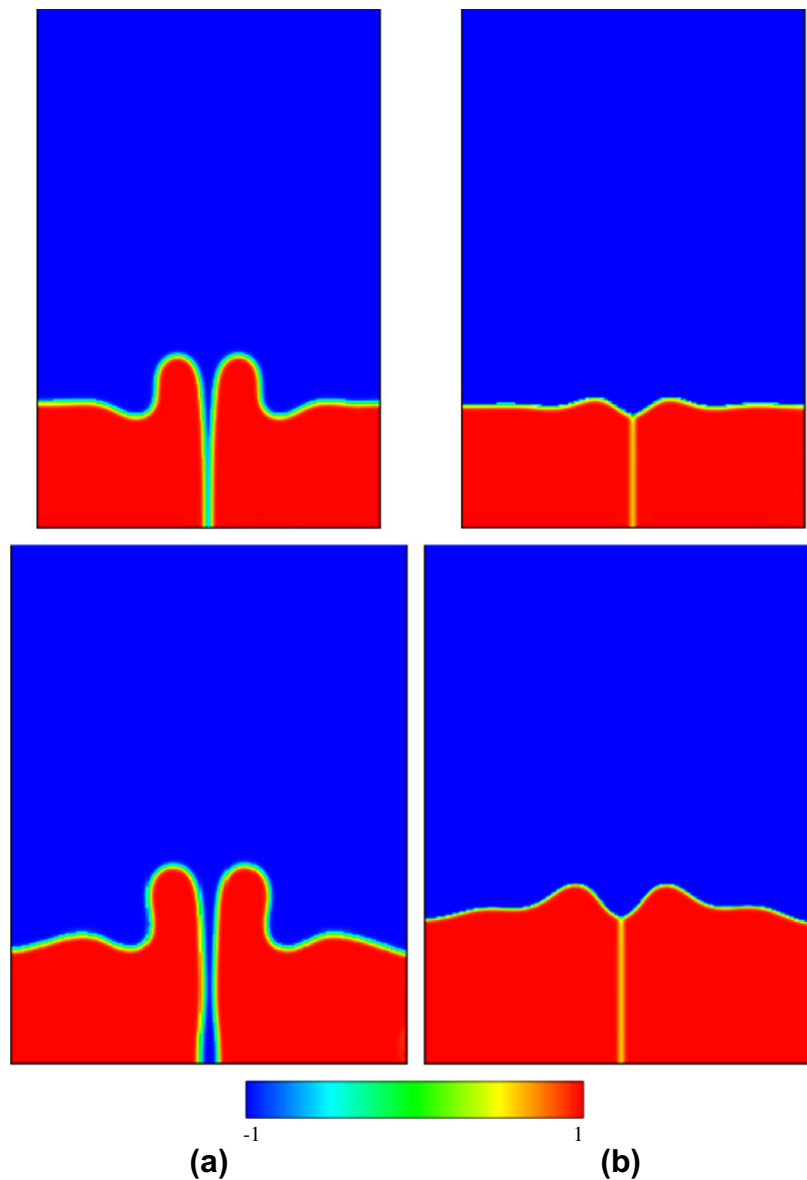


Fig. 4. Computed phase-field contours for solidification and tensile deformation of two adjacent misoriented grains in an undercooled melt. The upper panels show the contours immediately before straining is commenced in the simulation. The lower panels show the contours after the lateral sidewalls are displaced outwards. (a)  $\Delta\alpha/\Delta\alpha_c = 1.39$ , (b)  $\Delta\alpha/\Delta\alpha_c = 0.13$ .

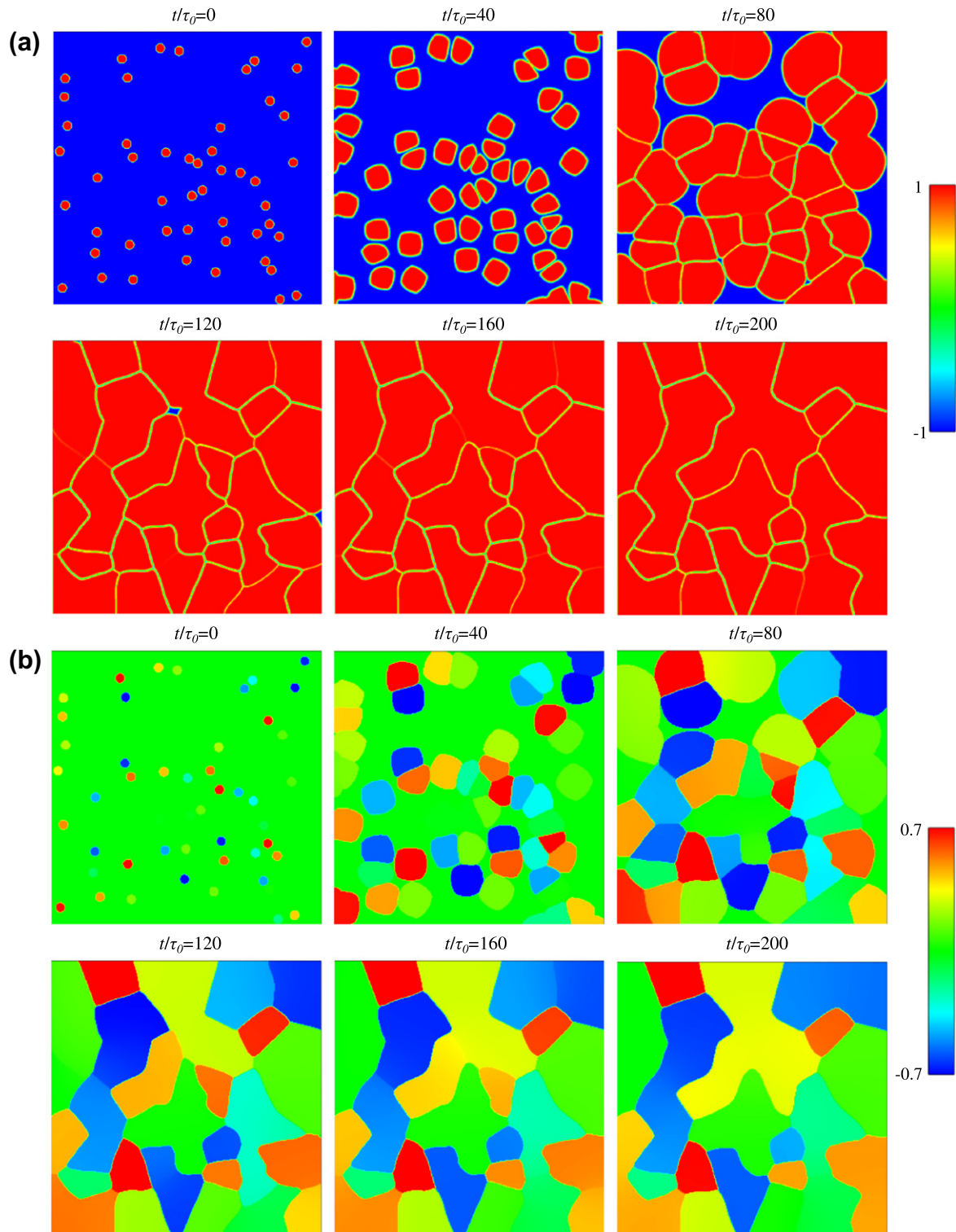


Fig. 5. Computed phase-field (a) and crystallographic orientation angle (b) contours for solidification and coarsening of multiple grains without deformation.

is fully wetted, i.e., the minimum value of the phase field within the grain boundary is equal to  $\phi = -1$  (fully liquid). For the lower misorientation ( $\Delta\alpha/\Delta\alpha_c = 0.13$ ), a finite dihedral angle forms at the junction between the liquid and the grain boundary, and the lowest value of the phase field within the grain boundary is positive ( $0 < \phi < 1$ ).

Beginning at the time corresponding to the upper panels in Fig. 4, the left and right side walls are displaced outwards, such that the total strain at the time corresponding to the lower panels of Fig. 4 is equal to 15%. The straining is performed over a relatively short time period, so that not much additional solidification occurs. In the stress analysis

that is performed during the straining period, the solid is assumed to be attached to the two vertical sidewalls, while frictionless sliding is allowed along the lower horizontal wall. The lower panels of Fig. 4 show that in the case of the wet grain boundary ( $\Delta\alpha/\Delta\alpha_c = 1.39$ ), the two grains are readily pulled apart. The stresses (not shown here) inside the grains are equal to zero. On the other hand, in the case of the dry grain boundary ( $\Delta\alpha/\Delta\alpha_c = 0.13$ ) with  $\phi > 0$  everywhere inside it, the grains remain attached as if they were a single solid structure. While this test case does not lend itself to a more quantitative evaluation of the deformation behavior, it serves to illustrate the present treatment of the mechanical behavior of a grain boundary.

### 3.3. Solidification and coarsening of multiple grains without deformation

In the third test case, the polycrystalline phase-field model is applied to simulate non-isothermal growth, impingement and coarsening of multiple grains in the absence of solid deformation. As shown in Fig. 5, 50 small circular solid seeds are randomly placed inside an undercooled liquid. The square computational domain has adiabatic boundaries and is discretized using  $1200 \times 1200$  node points (with a uniform spacing of  $\Delta x/W_0 = 0.4$ ). The initial melt undercooling and the crystalline anisotropy strength are taken as  $\theta_i = -0.55$  and  $\varepsilon = 0.05$ , respectively. The initial crystallographic orientation angle for each solid seed is also assigned randomly, but it is limited to the range  $-\pi/4 \leq \alpha \leq \pi/4$ . The heat sink term in Eq. (3) is activated at  $t/\tau_0 = 50$ , using  $c = 10/\tau_0$  and  $\theta_0 = -0.2$ . All other model parameters are set at the values provided in Section 2.

Fig. 5 shows six snapshots of the computed phase field and orientation angle contours up to  $t/\tau_0 = 200$ . At  $t/\tau_0 = 40$ , most of the grains have grown to a size large enough that they start to thermally interact. A few closely spaced grains have impinged upon each other and established grain boundaries. None of the grains appears dendritic because their spacing is too small for side arms to develop. Nonetheless, the four-fold crystalline anisotropy is apparent from the non-circular shape of the grains. At

$t/\tau_0 = 80$ , most of the domain is solidified. Already, the number of distinct grains has decreased from 50 to 34. This coarsening process can be attributed to grain boundary motion and grain rotation. The grains that have merged had a relatively low initial orientation mismatch. In the case of a large orientation mismatch between two impinging grains, the grain boundary is more stable. The coarsening process continues during the time period that the domain is fully solidified (starting at about  $t/\tau_0 = 120$ ). At  $t/\tau_0 = 200$ , the domain contains only 17 grains, with several of them about to merge. These grains have widely differing sizes and shapes. Overall, this test simulation demonstrates that the polycrystalline phase-field model of Warren et al. [12] is correctly implemented in the present study. The results are very similar to the 2-D solutions presented in Ref. [12].

## 4. Results and discussion

Three examples are presented where the coupled solidification and solid deformation of polycrystalline structures are simulated. The first example involves shear deformation of a polycrystalline globular structure, while the second and third examples deal with deformation of dendritic structures. Unless otherwise noted, all simulations use the model parameters stated in Section 2.

### 4.1. Shearing of a polycrystalline globular structure

As shown in the upper panels of Fig. 6, 14 globular seeds are placed in a staggered arrangement inside a rectangular domain ( $900 \times 150$  nodes) with adiabatic boundaries. Five seeds each are located along the bottom and top walls, while four seeds are positioned along the horizontal center line. The orientation angle of each seed crystal is assigned randomly. Crystalline anisotropy is not considered ( $\varepsilon = 0$ ). The initial temperature of the undercooled melt surrounding the seeds is set to  $\theta_i = -0.55$ . The lower panels of Fig. 6 show the computed phase-field and orientation angle contours at a time when the grains are impinging and forming grain boundaries. Depending on the misorientation of the grains with respect to each other, the mini-

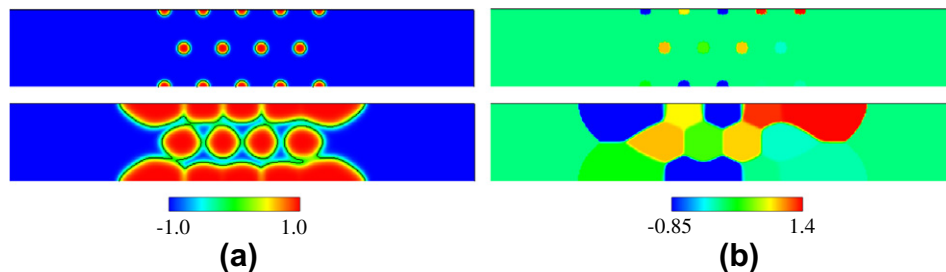


Fig. 6. Initial (without deformation) evolution of the phase field (a) and crystallographic orientation angle (b) contours for solidification of multiple globular grains inside an undercooled liquid. The upper panels correspond to the initial condition, while the lower panels are for a time in the simulation when a mechanically continuous solid structure across the height of the domain has just been established (the black line indicates the zero phase-field contour).

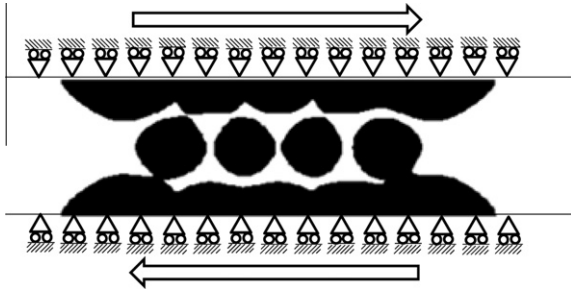


Fig. 7. Mechanical boundary conditions for the simulation of coupled solidification and shear deformation of a polycrystalline globular structure.

imum value of the phase field inside the grain boundaries varies widely. Recall that the zero phase-field contour (indicated as a black solid line in Fig. 6) is used in the stress model to differentiate between liquid- and solid-like mechanical behavior of a grain boundary. The lower panels of Fig. 6 correspond to the time when a (mechanically) continuous solid structure across the height of the domain has just been established. This solid bridge between the upper and lower row of grains is formed by the left-most grain in the center row. The right-most grain in the center row is (mechanically) merged with the bottom row of grains, but not yet with the top row.

Shear deformation of the polycrystalline structure is initiated at the time corresponding to the lower panels of Fig. 6. The mechanical boundary conditions for the stress analysis are illustrated in Fig. 7. The upper and lower walls of the domain are translated at a constant speed to the right and left, respectively. The translation speed is chosen low enough that during the shearing, considerable additional solidification occurs (see below). Since the present stress simulations neglect viscous effects (see Section 2), the computed stresses and strains are independent of the strain rate. In the following, a 10% (20%, etc.) shear implies a translation of both the upper and lower walls by an

amount equal to 10% (20%, etc.) of the height of the domain.

Fig. 8 shows four snapshots of the computed von Mises stress and equivalent plastic strain contours in the solid, while Fig. 9 provides the corresponding phase-field and orientation angle contours. The four rows of panels in each figure correspond to 0%, 10%, 20% and 40% shear. Already at 10% shear, the yield stress is reached in the thin solid bridges between the four center grains and the layers of grains along the top and bottom walls. The plastic deformations are limited to these thin bridges and do not affect the crystallographic orientation angles inside the grains. Inside the grains, the computed stresses show a complex distribution, but are still in the elastic range. For higher shear percentages, the plastic strains in the thin bridges connecting the center row of grains to the solid layers along the top and bottom walls continue to increase and reach values as high as 100% at 20% shear. At 40% shear, all of the grains are merged and form a continuous, fully solid structure (Fig. 9a). Coarsening has resulted in only five distinct grain orientations (Fig. 9b). Now, the stresses are approaching the yield stress over the entire center portion of the solid, but the plastic deformations are still limited to two narrow shear bands corresponding to the original grain boundaries between the center row of grains and the solid layers along the top and bottom walls (Fig. 8). The interior portions of the grains are essentially undistorted and hence the shearing has almost no effect on the crystallographic orientation of the grains. These results demonstrate clearly that deformation of a polycrystalline semi-solid structure occurs primarily due to plastic strains inside or near the grain boundaries. This localization of the strain in the grain boundary regions was also observed by Sistaninia et al. [11] in their granular model of mush deformation. Nonetheless, an improved description of the mechanical behavior of grain boundaries, which takes into account the local crystalline order, should be the primary aim of future studies in this regard.

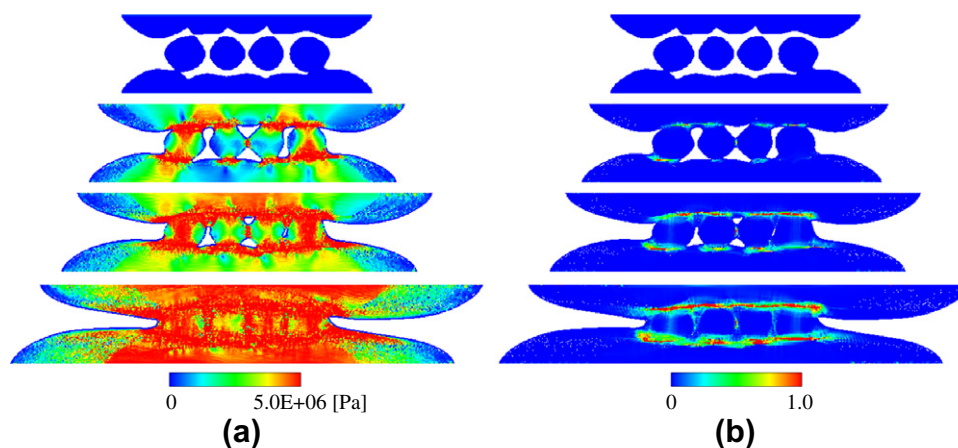


Fig. 8. Computed von Mises stress (a) and equivalent plastic strain (b) contours in the solid during the coupled solidification and shear deformation of a polycrystalline globular structure. From top to bottom, the rows of plots correspond to 0%, 10%, 20% and 40% shear.

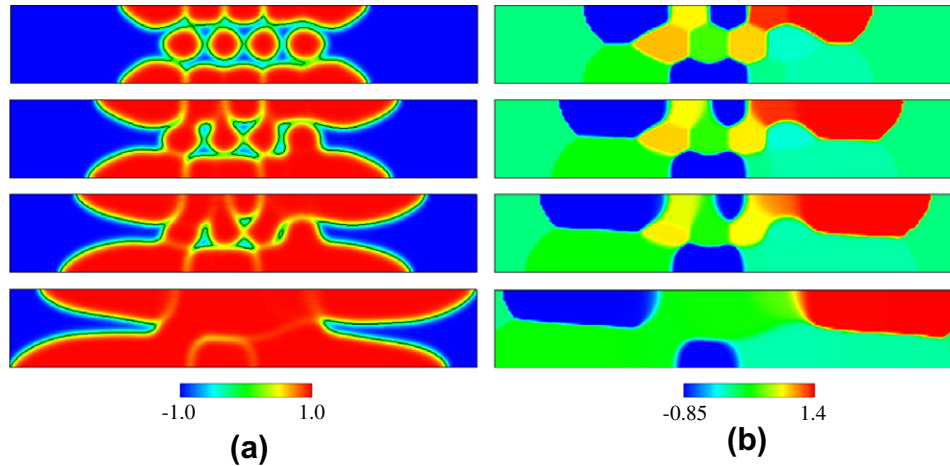


Fig. 9. Computed phase-field (a) and crystallographic orientation angle (b) contours during the coupled solidification and shear deformation of a polycrystalline globular structure. The black line in (a) indicates the zero phase-field contour. From top to bottom, the rows of plots correspond to 0%, 10%, 20% and 40% shear.

#### 4.2. Shearing of a dendritic crystal

This example is similar to the one in the previous section, except that a single dendritic crystal, instead of a polycrystalline globular structure, is sheared. Initially, three seeds having the same crystallographic orientation ( $\alpha = 0$ ) are placed along the bottom wall of the domain ( $1200 \times 200$  nodes). The initial melt undercooling is taken as  $\theta_i = -0.8$  and the crystalline anisotropy strength is set to a relatively high value of  $\varepsilon = 0.08$ . In addition, a thermal noise term is introduced into Eq. (2), following the procedure developed by Karma and Rappel [17]. As in the companion paper [3], the strength of the noise was chosen such that side branches develop during the growth of the dendrite. All other simulation parameters are the same as in the first example (Section 4.1). As can be seen in the upper panel of Fig. 10a, the seeds evolve into a complex dendritic structure with numerous relatively slender sidearms. The dendrite is a single crystal, since the orientation angle is the same everywhere (Fig. 10b). At the time corresponding to the first row of plots in Fig. 10, the dendritic crystal touches the upper wall of the domain and shearing is initiated. The shearing is accomplished by translating the upper and lower domain walls to the right and left, respectively, using the same mechanical boundary conditions as in the first simulation example (Fig. 7).

The four rows of panels in Fig. 10 show the computed phase-field and crystallographic orientation angle contours at 0%, 15% and 30% shear. The corresponding von Mises stress and equivalent plastic strain contours in the solid are displayed in Fig. 11. At 15% shear, the continuous layers of solid along the upper and lower domain walls have reached the yield stress and are deforming plastically (Fig. 11). The plastic strain is mostly limited to horizontal shear bands at the relatively thin junctions between the three vertical dendrite arms and the solid layers along the horizontal walls. Several shear bands are also present in

the solid directly adjacent to the moving horizontal walls. The stresses propagate into the three vertical dendrite arms, but most of the center portion of the dendrite does not yield. At 30% shear, the solid has continued to grow and deform, but the overall stress and plastic strain patterns are similar to the ones at 15% shear. Some of the higher order dendrite arms from the horizontally growing dendrite branches in the center of the domain are beginning to form bridges to the solid layers along the top and bottom walls. These very small bridges are also yielding. In summary, during shearing of a single crystal, the strain is generally localized in thin shear bands that are located in the thin junctions between dendrite branches.

The computed deformations of the solid have a profound effect on the crystallographic orientation angle field in the dendrite, as displayed in Fig. 10b. The shearing causes several distinct sub-grains to form within the solid layers along the top and bottom walls. The formation of the sub-grain boundaries can be explained by the standard tilting mechanism. The sub-grain boundaries in the solid layers along the top and bottom walls can all be characterized as low angle, since the misorientations between the sub-grains are always much below  $\Delta\alpha \approx 0.2$  ( $\approx 11^\circ$ ). Furthermore, the values of the phase field inside the sub-grain boundaries remain very close to unity (Fig. 10a), implying that in the present stress model the solid layers along the top and bottom walls behave mechanically as a single solid structure. Over time, the sub-grains undergo some coarsening, but the shearing continues to create new sub-grains. High-angle grain boundaries can be observed between some of the sub-grains in the solid layers and the horizontally growing dendrite branches in the center of the domain, which are essentially undistorted ( $\alpha = 0$ ). Hence, in addition to the formation of tilt grain boundaries inside individual dendrite arms, impingement of different arms of a deformed single dendrite can also lead to grain boundaries. While these phenomena are well known in the man-

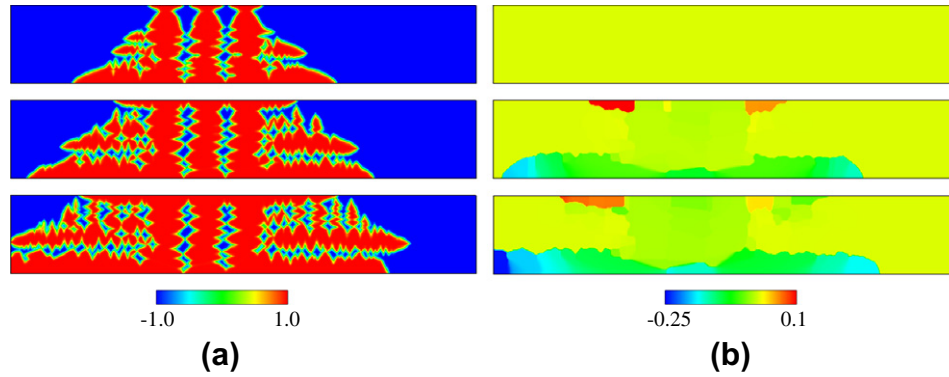


Fig. 10. Computed phase-field (a) and crystallographic orientation angle (b) contours during the coupled solidification and shear deformation of a dendritic crystal. From top to bottom, the rows of plots correspond to 0%, 15% and 30% shear.

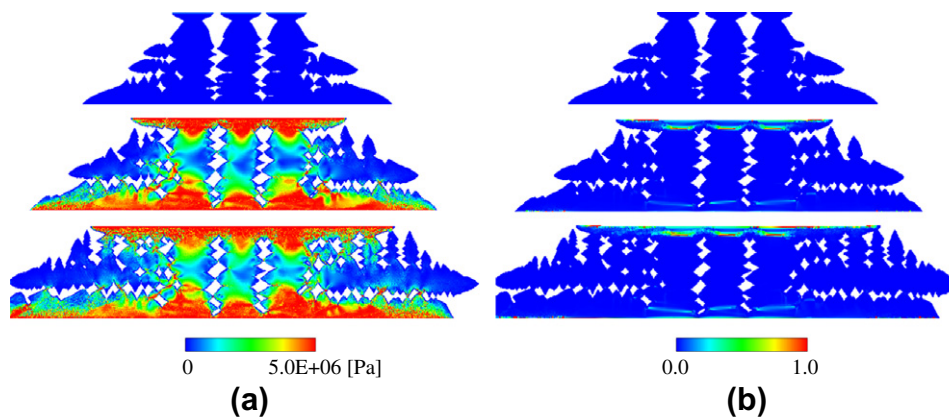


Fig. 11. Computed von Mises stress (a) and equivalent plastic strain (b) contours in the solid during the coupled solidification and shear deformation of a dendritic crystal. From top to bottom, the rows of plots correspond to 0%, 15% and 30% shear.

ufacture of single crystals, they have not been simulated previously.

#### 4.3. Compression of a dendritic network

The third simulation example involves compression of a single crystal dendritic network at a high volume fraction of solid. Initially, a single seed with  $\alpha = 0$  is placed in the lower left corner of a rectangular domain ( $1200 \times 600$  nodes) with adiabatic boundaries. The dendritic growth conditions are the same as in the previous example (Section 4.2). After some time, the vertically growing dendrite arm along the left wall reaches the upper boundary of the domain. As shown in Fig. 12, at that time a complex single-crystal dendritic network is established over much of the domain and compression is initiated. Inside the dendritic network, the solid fraction is  $\sim 80\%$ . During the compression, the upper domain wall is moved downward, while frictionless sliding is allowed along all other walls (Fig. 12). The compression rate is chosen such that at 20% compression, the horizontally growing dendrite arm along the lower domain wall increases in length by  $\sim 150\%$ .

Fig. 13 shows the computed phase-field and crystallographic orientation angle contours at 0%, 5%, 10% and

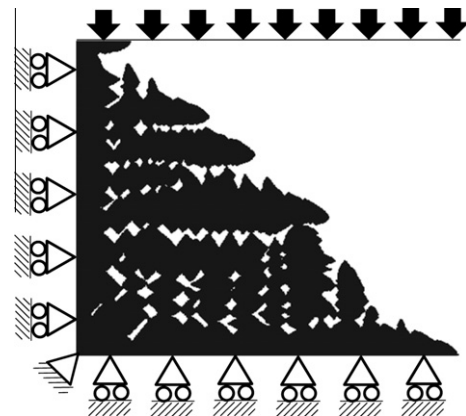


Fig. 12. Mechanical boundary conditions for the simulation of coupled solidification and compression of a dendritic network.

20% compression. The corresponding von Mises stress and equivalent plastic strain contours in the solid are displayed in Fig. 14. It can be seen that the yield stress in the solid is first reached in the upper left corner of the domain. With increasing compression, the region of plastic deformation propagates downwards and to the right inside the dendrite arms that are directly adjacent to the left ver-

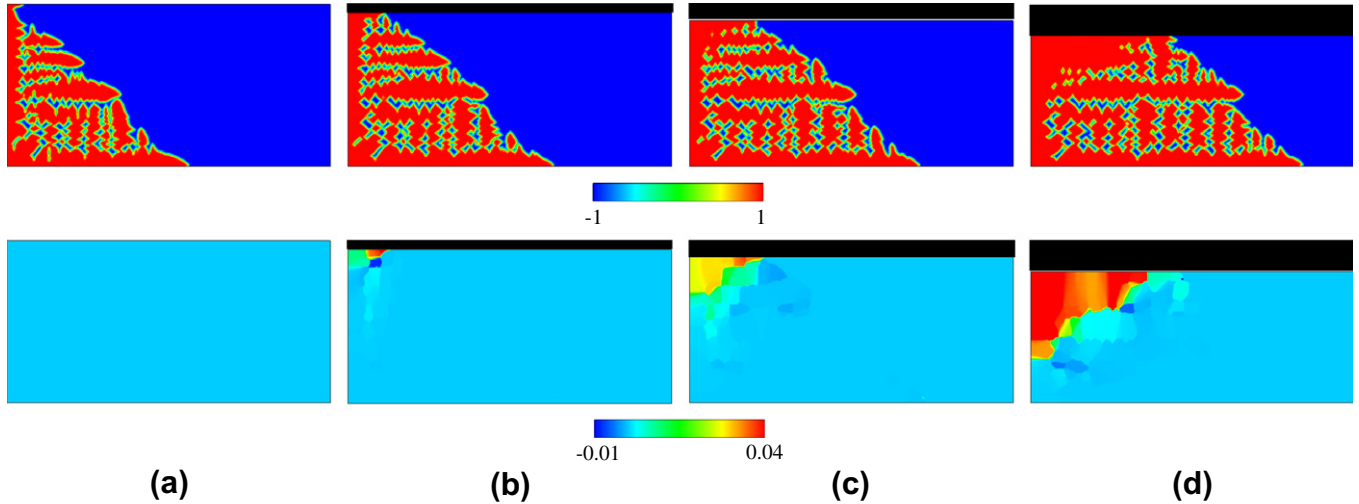


Fig. 13. Computed phase-field (upper row) and crystallographic orientation angle (lower row) contours during the coupled solidification and compression of a dendritic network. (a) 0% compression, (b) 5% compression, (c) 10% compression, (d) 20% compression.

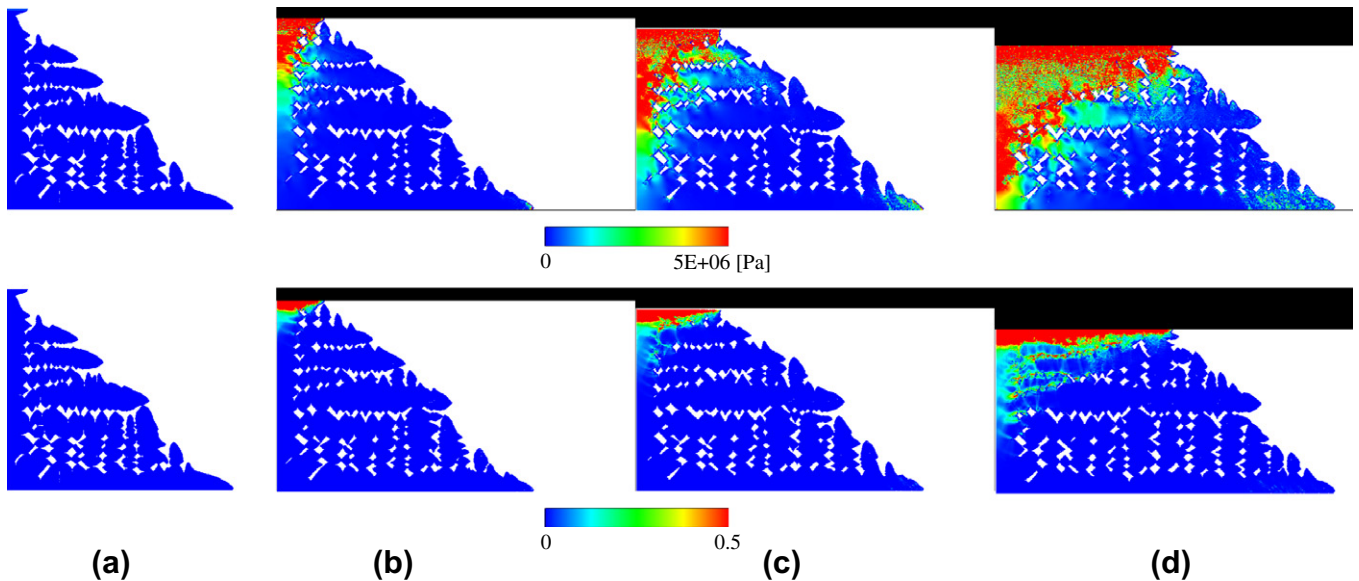


Fig. 14. Computed von Mises stress (upper row) and equivalent plastic strain (lower row) contours in the solid during the coupled solidification and compression of a dendritic network. (a) 0% compression, (b) 5% compression, (c) 10% compression, (d) 20% compression.

tical and upper horizontal domain walls. The compression causes some of the interior dendrite arms in the upper portion of the domain to impinge and merge. Yielding can be observed in the relatively thin rows of bridges between impinging dendrite arms. At 20% compression, a continuous, fully solid region exists in approximately the upper 25% of the solid network (upper panels of Fig. 13). On the other hand, the dendrite arms in the lower portion of the domain are essentially undeformed. The lower panels of Fig. 13 indicate that the plastic deformation of the dendritic network causes again the formation of numerous sub-grains that are separated by low-angle grain boundaries. As in the previous example, these grain boundaries exist both within individual dendrite arms and between deformed dendrite arms that have impinged.

In summary, the present simulation shows that compression of a relatively homogeneous, single crystal and high solid fraction dendritic network results in highly inhomogeneous deformations. The deformations are limited to a relatively thin layer along the compressing boundary. The compression causes consolidation of the dendritic network in this layer into a fully solid structure that consists of numerous sub-grains.

## 5. Conclusions

A model is developed to numerically simulate coupled solidification and deformation of polycrystalline structures. Solidification and grain boundary dynamics are modeled using the polycrystalline phase-field model of Warren

et al. [12]. This model is modified to account for the advection of the phase-field, temperature and crystallographic orientation angle by solid deformation. The stresses and elasto-viscoplastic strains (all simulations in this paper neglect viscous effects) in the solid are computed using the material point method [6]. The flow field in the liquid phase is approximated through a zero-gradient extension of the solid velocities. The mechanical behavior of a grain boundary is modeled using a highly approximate procedure that is based on the local value of the phase field. Fully solid behavior is assumed when  $\phi > 0$  everywhere inside a grain boundary. Conversely, for values of  $\phi < 0$ , the grain boundary is assumed to contain sufficient liquid-like material that no stresses are transmitted. The present implementation of the polycrystalline phase-field model is validated in several numerical tests.

Three examples are presented to demonstrate the suitability of the present model to simulate the coupled solidification and deformation of polycrystalline structures. It is shown that shearing of a semi-solid structure occurs primarily in relatively narrow bands near or inside the grain boundaries or the thin junctions between different dendrite arms. The deformations can cause the formation of low-angle tilt grain boundaries inside individual dendrite arms. In addition, grain boundaries form when different arms of a deformed single dendrite impinge. During compression of a high-solid fraction single crystal dendritic structure, the deformations are limited to a relatively thin layer along the compressing boundary. The compression causes consolidation of this layer into a fully solid structure that consists of numerous sub-grains.

Before the present model can be applied to study the mechanical behavior of metal alloys in the semi-solid state, several improvements are needed. The most obvious change needed is a better model for the mechanics of grain boundaries. Such a model should take into account the dependence of the mechanical behavior on the local crystalline order as reflected by the phase field,  $\phi$ . In this respect, it would be highly desirable to develop unified mechanical constitutive relations that are valid for any

value of the phase field, spanning all the way from fully liquid ( $\phi = -1$ ) to fully solid ( $\phi = +1$ ). This would also enable the simultaneous modeling of the flow in the liquid phase. Three-dimensional simulations are possible, because three-dimensional versions of both the polycrystalline phase-field model [18] and the material point method [19] are available. However, such simulations would require large computer resources. Last, but not least, the parameters in the polycrystalline phase-field model should be adjusted to more closely correspond to real materials.

### Acknowledgement

This work was financially supported, in part, by NASA under Grant Number NNX10AV35G.

### References

- [1] Dantzig JA, Rappaz M. Solidification. Lausanne: EPFL Press; 2009.
- [2] Pokorny MG, Monroe CA, Beckermann C, Zhen Z, Hort N. *Metall Mater Trans A* 2010;41:3196.
- [3] Yamaguchi M, Beckermann C, submitted for publication.
- [4] Kobayashi R. *Physica D* 1993;63:410.
- [5] Boettinger WJ, Warren JA, Beckermann C, Karma A. *Ann Rev Mater Res* 2002;32:163.
- [6] Sulsky D, Chen Z, Schreyer HL. *Comput Method Appl Mech Eng* 1994;118:179.
- [7] Farup I, Drezet JM, Rappaz M. *Acta Mater* 2001;49:1261.
- [8] Terzi S et al. *Scripta Mater* 2009;61:449.
- [9] Phillion AB, Cockcroft SL, Lee PD. *Acta Mater* 2008;56:4328.
- [10] Fuloria D, Lee PD. *Acta Mater* 2009;57:5554.
- [11] Sistaninia M, Phillion AB, Drezet JM, Rappaz M. *Metall Mater Trans A* 2011;42:239.
- [12] Warren JA, Kobayashi R, Lobkovsky AE, Carter WC. *Acta Mater* 2003;51:6035.
- [13] Karma A, Rappel WJ. *Phys Rev E* 1998;57:4323.
- [14] Gibou F, Fedkiw RP, Cheng L, Kang M. *J Comput Phys* 2002;176:205.
- [15] Benson DJ. *Comput Method Appl Mech* 1992;99:235.
- [16] Takewaki H, Nishiguchi A, Yabe T. *J Comput Phys* 1985;61:261.
- [17] Karma A, Rappel WJ. *Phys Rev E* 1999;60:3614.
- [18] Kobayashi R, Warren JA. *Physica A* 2005;356:127.
- [19] Gilmanov A, Acharya S. *Int J Numer Meth Fluid* 2008;56:2151.